Journal of Catalysis 267 (2009) 67–77

Contents lists available at ScienceDirect

Journal of Catalysis

journal homepage: www.elsevier.com/locate/jcat

Temperature-programed reduction of unpromoted MoS_2-based hydrodesulfurization catalysts: Experiments and kinetic modeling from first principles

Nicolas Dinter [a], Marko Rusanen [a], Pascal Raybaud [b], Slavik Kasztelan [b], Pedro da Silva [b], Hervé Toulhoat [c,*]

[a] Direction Chimie et Physico-Chimie Appliquées, IFP, 1 & 4 Avenue de Bois-Préau, 92852 Rueil-Malmaison Cedex, France
[b] Direction Catalyse et Séparation, IFP, Rond-point de l'échangeur de Solaize BP 3, 69360 Solaize, France
[c] Direction Scientifique, IFP, 1 & 4 Avenue de Bois-Préau, 92852 Rueil-Malmaison Cedex, France

ARTICLE INFO

Article history:
Received 27 May 2009
Revised 28 July 2009
Accepted 31 July 2009
Available online 31 August 2009

Keywords:
Density functional theory
HDS catalysts activation
Kinetic modeling
Temperature-programed reduction

ABSTRACT

In this report, we have addressed the mechanism of reduction of sulfided γ-Al_2O_3 supported MoS_2 catalytic nanoparticles by dihydrogen gas, starting from the state 100% sulfur covered and ending in 50% sulfur covered Mo-edges, with the production of gaseous hydrogen sulfide. We have prepared and characterized a consistent set of oxidic catalysts precursors with variable loadings in Mo, presulfided these catalysts under high chemical potential of sulfur, ensuring prevalence of 100%S covered Mo-edges (triangular nanoparticles), and finally acquired temperature-programed reduction (TPR) spectra. We have performed DFT calculations of the free-energy barriers along the reduction pathway, elaborated analytical models of TPR spectra with free-energy activation barriers and some measurable catalysts characteristics as inputs, and discriminated among various sticking coefficient models with respect to the experimental data. We find that the rate-determining step for the onset of reduction is the dissociative chemisorption of H_2 on two adjacent capping S_2 dimers yielding mono-sulfhydrilated S_2 pairs in mutual hydrogen bonding situations, with a free-energy barrier of 1.5 eV. The observed decrease of TPR spectra peak temperatures with increasing Mo content results from an increase in the ratio of the area available for reactive adsorption over the total surface area as the loss of dispersion is overcompensated by the increasing active Mo-edge area.

1. Introduction

In view of the accumulated amount of experimental and theoretical research devoted to these intriguing and strategic materials, in particular over the past thirty years [1,2], hydrotreatment catalysts are today probably the best described among heterogeneous catalysts used by the oil refining industry. Indeed, subject to a strong competitive pressure, these rather mature commodities have followed a kind of evolutionary process leading to a situation in which whatever the manufacturer, a robot portrait can be drawn of all catalysts in the market. In the optimal activated state, they work as nanoparticles (average main diameter 2–4 nm) of lamellar chalcogenides (MoS_2, WS_2), often dispersed as singled S–M–S sheets, but on average stacked by 1–2, in loose interaction with the supporting ultrapure γ-alumina nanoplatelets. Active sites are located at nanosulfide particle edges [3–5], and activities may be enhanced by a factor of order 1000 by Ni or Co. As clearly shown recently by first principles computer simulations [6,7], and STM experiments [4,8–10], these "promoters" preferably sit at edges, substituting in the formal +2 oxidation state to Mo^{4+} or W^{4+} edge ions. According to EXAFS and STM experiments [4,11–13], and recent computer simulations [14,15], edge cations coordination numbers by S^{2-} anions at equilibrium depend primarily on the local chemical potential of sulfur and cation nature. Symmetry imposes that nanosized MoS_2 or WS_2 crystallites exhibit, besides the majority basal planes, two type of edges, generally denoted as Mo-edge $(1\,0\,\bar{1}\,0)$ and S-edge $(\bar{1}\,0\,1\,0)$, the ratio of which, and hence the nanoparticle aspect ratio, is also controlled by chemical potential of sulfur and nature of promoters. The so-called "synergetic" effect of promoters (Ni, Co) on base transition elements (Mo, W) in these peculiar systems is now well understood in terms of periodic trends in the hydrodesulfurization (HDS) activity of transition metal sulfides (TMS) [16,17]: in accordance with the principle of Sabatier [18], an optimal metal–sulfur bond strength (E_{MS}) exists which maximizes activity in given operating conditions [19].

Such a wealth of details and answers calls for many new questions, fundamental and of broad range for heterogeneous catalysis. Among them is that of the precise mechanism of dihydrogen activation by TMS in general, and nanosized MoS_2-based catalysts in

* Corresponding author. Fax: +33 (0)1 47 52 70 22.
E-mail address: herve.toulhoat@ifp.fr (H. Toulhoat).

0021-9517/$ - see front matter © 2009 Elsevier Inc. All rights reserved.
doi:10.1016/j.jcat.2009.07.017

particular. DFT based "Ab Initio Atomistic Thermodynamics" (AIAT) [20–22] predicts, for comparison to experiment, equilibrium speciations and conformations at a finite temperature, as functions of chemical potentials of elements involved. Assuming that the working catalyst's surface remains close enough to equilibrium, its best atomistic model, as a starting point, is provided by AIAT, which is, however, unable to provide the dynamic picture. Potential energy profiles along reaction coordinates for given elementary molecular reactions at model surfaces can be established using DFT. Local minima and saddle points can be localized on such surfaces, corresponding to chemisorbed reactants and products connected by transition states, allowing reaction energies and barriers to be evaluated as differences in energy levels.

In this report we present a combined experimental and first principles theoretical study of MoS_2 Mo-edge activation by dihydrogen. On the experimental side, γ-alumina supported catalysts with Mo loading varying in the range 4–22 wt% are presulfided in conditions leading to dispersed triangular nanocrystallites presenting only S_2 dimers capped Mo-edges (100% initial coverage by S). These catalysts are then subjected to temperature-programed reduction (TPR) by dihydrogen in a differential isothermal fixed bed, while monitoring H_2 consumption and H_2S production. TPR spectra (i.e. consumption/production rates versus temperature) present a narrow low temperature peak, culminating in the range 520–560 K, depending on Mo loading, and a broad peak in the range 700–1000 K. We concentrate on the interpretation of the first narrow peak, through a modified Redhead model.

The paper is organized as follows: the "Methods" section is subdivided into "Experimental" and "Theoretical" methods. Experimental methods comprise the description of catalysts preparation, characterization, presulfidation, and TPR. Theoretical methods comprise descriptions of:

- The models used to compute rates of elementary events, with special emphasis on different descriptions of dissociative adsorption that can be considered.
- The set of approximations and choice of parameters adopted for DFT calculations of energy barriers.
- The basic assumptions and related formulas for our modified version of the Redhead model of temperature-programed reduction spectra.

In the "Results" section, we present first catalyst characterization results, then experimental TPR spectra followed by DFT results for the free-energy profile along the S_2 dimers reduction pathway. This is followed by the comparison, with respect to the experimental results, of kinetic models that could be implemented in the modified Redhead analysis, allowing to select the most consistent model for dissociative adsorption of H_2.

The discussion is focussed on the consistency between experiment and DFT-based modified Redhead analysis, including possible error sources in experiments and modeling and the merits of alternative interpretations. From this discussion we draw conclusions concerning H_2 activation by MoS_2-based catalysts.

2. Methods

2.1. Experiments

2.1.1. Catalysts preparation

Seven catalysts with varying Mo contents were prepared according to the Incipient Wetness Impregnation method using solutions of ammonium heptamolybdate (Merck ultrapure) in distilled water, and ultrapure γ-alumina extrudates (GFSC Rhone-Poulenc) as pre-formed catalyst support. The characteristics of the latter are given in Table 1. The impregnated extrudates were allowed to maturate 3 h under water saturated atmosphere at ambient temperature, then gently dried overnight at 400 K. Dried samples were finally calcined under flowing dry air for 2 h at 773 K leading to catalyst precursors under the oxidic form. In the case of Mo contents larger than 10 wt% on the final catalysts, about 5 vol.% of H_2O_2 from a 30 vol.% aqueous solution was added to impregnation solutions in order to increase heptamolybdate solubility. Moreover, for Mo contents over 14%, the impregnation was conducted in two stages with an intermediate calcination under flowing dry air for 2 h at 623 K.

Table 1
Support characteristics (GFSC from Rhône-Poulenc).

Shape	1.2 mm extrudates
Specific surface	227 m^2/g
Grain density	0.95 g/cm^3
Structural density	3.31 g/cm^3
Porous volume	0.75 cm^3/g

2.1.2. Catalysts characterization

Surface areas were measured by N_2 adsorption at 77 K, according to the B.E.T. method. Grain densities and total pore volumes were measured by Helium picnometry. Total Mo contents in the final oxidic catalyst precursors were determined by X-Ray Fluorescence (XRF) with a Philips PW 1404 (tungsten anticathode) or a Philips 1480 (scandium/molybdenum anticathode) apparatus. In order to assess the homogeneity of preparations, radial distribution of Mo across extrudates cross-sections was determined with a CAMECA Castaing microprobe. To verify the absence of crystallized MoO_3, indicative of poor Mo dispersion, X-ray diffraction experiments were performed on mortar gently ground oxidic catalysts precursors with a Philips PW 1820 X-ray diffractometer, equipped with a cobalt anode and a graphite rear monochromator. Transmission Electron Microscopy (TEM) analysis of sulfided catalysts were performed with a JEOL 2010 (point resolution 0.2 nm) and a JEOL 120CX (point resolution 0.3 nm) in order to evaluate MoS_2 nanoparticles distribution of sizes and stacking degrees. To this end, fields of size 100×100 nm were randomly selected across the preparations and electron micrographs recorded in order to maximize contrast revealing MoS_2 slabs as dark fringes (absorbing Mo (001) planes). Circa 300 slabs per sample were identified in order to construct histograms of length and stacking degree (see Supplementary material). X-ray Photoelectron Spectroscopy (XPS) studies were performed with a Kratos XSAM 800 spectrometer, on both the oxidic precursors and sulfided catalysts, in order to evaluate the distribution of surface Mo species according to their oxidation state. The Al K_α line at 1486.7 eV was used as X-ray source. Binding energies were referred to Al 2p at 74.6 eV. Sulfided catalysts were prepared in a glove box under flowing Helium. Sulfided samples were ground under He in a porcelain mortar, then a thin layer of the resulting powder was pressed on a sample holder and was covered with an Indium sheet. Prepared sulfided samples were then transferred without any air exposure into the analysis chamber where analysis was performed under secondary vacuum.

2.1.3. Temperature-programed reduction

Temperature-programed reduction experiments were performed dynamically in a vertical downflow isothermal differential quartz reactor, with a modified multifunctions χsorb apparatus licensed to GIRA by IFP. H_2 content in inlet and outlet gas was measured with a Thermal Conductivity Detector (TCD) and H_2S content with a Flame Photometry Detector (FPD). A standard protocol was applied to all catalysts, involving first an in situ sulfidation of oxidic dry precursors, under 20 cm^3STP min^{-1} of a (H_2 + 15%molH_2S)

mixture: starting from ambient, the temperature program started by a ramp of linearly increasing temperature by 5 °C min^{-1} up to 400 °C, followed by 2 h at 400 °C, followed by 45 min under 20 cm^3STP min^{-1} of a (N_2 + 15%mol H_2S) mixture, and finally, cooling under the same flowing mixture down to 50 °C. The final step of this sulfiding procedure ensured theoretically the preparation of supported triangular MoS_2 nanocrystallites expressing only 100%S covered Mo-edges [15,49,50].

The TPR experiment followed, starting by flushing the reactor and lines with 25 cm^3STP min^{-1} pure Argon for 20 min, then with 25 cm^3STP min^{-1} (Ar + 5%mol H_2) for 40 min, followed by linear temperature increase at 10 °C min^{-1} up to 900 °C under the same gas flow, while monitoring continuously H_2 consumption and H_2S production across the catalyst bed by coupled TCD–FPD. After this TPR stage, the catalyst was maintained 1 h at 900 °C under the flowing reducing mixture, then cooled down to ambient temperature.

2.2. Simulations

2.2.1. Representation of elementary steps

Catalytic systems under consideration involve solid surfaces described by an array of "sites", and exposed to a gas mixture composed of different species i with masses m_i. In what follows, gas phase is assumed ideal and fully described with partial pressures P_i and temperature T. Relevant processes occurring on these surfaces are adsorptions, desorptions, diffusions, and chemical reactions.

Adsorption may be considered as proceeding in two consecutive steps, (i) unactivated physisorption and (ii) activated chemisorption. The corresponding consecutive reverse steps will lead to desorption. In what follows, subscript letters g, ϕ, and χ denote, respectively, the gaseous, physisorbed, and chemisorbed states. When connected by an arrow, e.g. $g \to \phi$, pairs of such letters refer to a process connecting two states, e.g. physisorption. The physisorption rate $k^{KTG}_{g\to\phi}$ depends on the kinetic impingement described by the kinetic theory of gases (*KTGs*). It can be written through Eq. (1), [23], with units of s^{-1}, where $f^{ad}(T) \leqslant 1$ stands for the sticking probability upon impingement, in general temperature dependent. It is approximated to unity in what follows. For one impinging particle, of mass m coming from a gas phase at pressure P, a total area of A_{uc} is available for physisorption (of the order of 10^{-19} in m^2 $site^{-1}$). k_B is the Boltzmann constant (J K^{-1}).

Considering the subsequent activated chemisorption step, let $\Delta G^{\neq}_{\phi\to\chi}$ denote the free-energy barrier to overcome on going from the free-energy minimum corresponding to the molecularly physisorbed state toward that corresponding to the chemisorbed, eventually dissociated state, passing by the saddle point corresponding to a transition state (TS). The enthalpic and entropic contributions $\Delta H^{\neq}_{\phi\to\chi}$ and $\Delta S^{\neq}_{\phi\to\chi}$ to $\Delta G^{\neq}_{\phi\to\chi}$ are distinguished in Eq. (2). These components can be computed from first principles for relevant atomistic models of the ϕ, χ, and TS states: let E_ϕ, E_χ, and $E^{\neq}_{\phi\to\chi}$ denote, respectively, the total electronic energies of these models at 0 K, and let and $\nu_{\phi,k}$, $\nu_{\chi,l}$, and $\nu^{\neq}_{\phi\to\chi,j}$ the corresponding sets of normal modes real frequencies computed in the harmonic or anharmonic approximations from the hessian matrices. We use the classical statistical mechanics formulae (see for instance [24]) to compute the vibrational, translational, and rotational components of entropies and enthalpies for any state, according to Eqs. (SI1)–(SI6).

$$k^{KTG}_{g\to\phi}(T,P) = f_{ad}(T)\frac{PA_{uc}}{\sqrt{2\cdot\pi\cdot m\cdot k_B\cdot T}} \tag{1}$$

$$\Delta G^{\neq}_{\phi\to\chi} = \Delta H^{\neq}_{\phi\to\chi} - T\Delta S^{\neq}_{\phi\to\chi} \tag{2}$$

Considering the dissociative adsorption of a small molecule like H_2 our H_2S, we assume that the rotational and translational components of entropy can be neglected for the transition state, but not for the physisorbed state. Eq. (3), fitted from the results of a DFT calculation of thermodynamic functions for H_2, provides the value of the sum of these components for dihydrogen in ideal gas phase at a function of temperature. For want of an adequate theoretical model for the physisorbed state, specifying exactly the loss of degrees of freedom on quasi 1 D Mo-edge surfaces, we assume that the translational-rotational entropy of physisorbed dihydrogen on the 100% S covered Mo-edge is a fraction f of that of the gaseous state at the same temperature. Recent experiments for the physisorption of diatomic gases on titanium silicate sorbents [25] indicate f is in those cases in the range 0.5–0.7 for O_2, N_2 or CH_4 at 273 K, and hardly changing with increasing temperature, but more sensitive to surface modifications (e.g. nature of cation exchanges in surface). In what follows, we assume f to be a function of temperature and S coverage θ_S, as expressed formally by Eq. (4).

$$S^{H_2,g}_{tra+rot}(T) = 26.19 + 0.016T \quad Cal.mol^{-1}.K^{-1} \tag{3}$$

$$S^{H_2,\phi}_{tra+rot}(T) = f[T,\theta_S]S^{H_2,g}_{tra+rot}(T) \quad 0 \leqslant f \leqslant 1 \quad Cal.mol^{-1}.K^{-1} \tag{4}$$

According to Eyring, Evans and Polanyi [26–28] transition state theory (TST), the chemisorption rate $k_{\phi\to\chi}$ is given by Eq. (5), with units of [s^{-1}]. The rate of the reverse process $k_{\chi\to\phi}$ follows Eq. (6).

$$k_{\phi\to\chi} = \frac{k_BT}{h}\exp\left(\frac{\Delta S^{\neq}_{\phi\to\chi}}{k_B}\right)\exp\left(-\frac{\Delta H^{\neq}_{\phi\to\chi}}{k_BT}\right) \tag{5}$$

$$k_{\chi\to\phi} = \frac{k_BT}{h}\exp\left(\frac{\Delta S^{\neq}_{\chi\to\phi}}{k_B}\right)\exp\left(-\frac{\Delta H^{\neq}_{\chi\to\phi}}{k_BT}\right) \tag{6}$$

The desorption rate from the physisorbed state $k_{\phi\to g}$, is linked to the physisorption rate according to the detailed balance equation (microscopic reversibility) Eq. (7), with $\Delta G_{g\to\phi}$ the free-energy variation associated to the physisorption process. For dihydrogen, using our approximation in Eq. (4), the latter quantity can be approximated by Eq. (8) where E_b is the physisorption energy.

$$k_{\phi\to g}(T,P) = k^{KTG}_{g\to\phi}\exp\left(\frac{\Delta G_{g\to\phi}(T,P)}{k_bT}\right) \tag{7}$$

$$\Delta G_{g\to\phi}(T,P) = E_b - T(1-f)S^{H2,g}_{tra+rot}(T) \tag{8}$$

The forward and backward barriers for the process leading to chemisorption from the physisorbed state, as used in Eqs. (5) and (6), are related by the free-energy change associated with this process, $\Delta G_{\phi\to\chi}$, according to Eq. (9):

$$\Delta G_{\phi\to\chi} = \Delta G^{\neq}_{\phi\to\chi} - \Delta G^{\neq}_{\chi\to\phi} \tag{9}$$

At this point, it is worth considering the various models proposed in the literature to describe dissociative adsorption: for this event, which is not elementary, one wants to express the local forward rate k_{da} as function of the previously defined rates of elementary processes $k^{KTG}_{g\to\phi}$ and $k_{\phi\to\chi}$. We have considered five different models, denoted in what follows H1, H1bis, H2, H3, and H4.

In general, the temperature dependent sticking coefficient $S_t(T)$ is defined as the ratio k_{da} to $k^{KTG}_{g\to\phi}$, Eq. (10).

$$k_{da} = St(T)k^{KTG}_{g\to\phi} \tag{10}$$

In all cases, the ratio of the area available for reactive adsorption to the total area available for adsorption A_{st}/A_{uc} comes as an adimensional prefactor in k_{da}. In the case of supported MoS_2 nanoparticles, we assimilate the total (macroscopic) area available (A_{uc}) for physisorption to the total specific area SA (m^2 g^{-1}) of the supported catalyst. The total area available for dissociative adsorption (A_{st}) is directly linked to the site area a_s (m^2) times the site density. The latter is the number of sites per gram of catalyst, or density of Mo edge sites θ_{Moe} (g^{-1}). Introducing the ratio α of Mo edge sites to Mo atoms involved in MoS_2 nanoparticles, the latter being approximated by

the Mo^{+4} (wt%) content as determined by XPS, α times Mo^{4+} is the number of Mo on MoS_2-edges. Using N_{Av}, the Avogadro number and M_{Mo}, the atomic weight of Molybdenum, one gets finally Eq. (11):

$$\left(\frac{A_{st}}{A_{uc}}\right) = \frac{\alpha M_o^{4+} N_{Av} a_s}{M_{Mo} SA} \tag{11}$$

Assimilating one site to a pair of capping S_2 dimers at the 100%S Mo-edge surface (since as shown below two dimers are involved in the dissociative adsorption of one H_2), the site area a_s is evaluated at 9×10^{-20} m^2. The surface area of the sulfided catalyst can be reasonably approximated by the surface area of support introduced in the experiment per gram of oxidic precursor, according to Eq. (12), where SSA is the support specific area and Mo is the measured molybdenum content in the oxidic precursor in weight percent, assuming a stoichiometry close to MoO_3.

$$SA = SSA\left(\frac{100 - (1.5Mo)}{100}\right) \tag{12}$$

Within model H1, one expresses the sticking coefficient $St(T)$ as proportional to the Boltzmann probability to overcome the activation barrier between the physisorbed and the chemisorbed state. In the crudest approximation, neglecting differences between the partition functions in the transition state and physisorbed states, the free energy of activation is merely approximated by the electronic energy barrier, and k_{da} is expressed by Eq. (13), with $k^{KTG}_{g\to\phi}$ following Eq. (1).

An improved formula makes use of Eq. (2) and we will refer in that case to model H1bis, Eq. (14).

$$k_{da} = k^{KTG}_{g\to\phi}\left(\frac{A_{st}}{A_{uc}}\right)\exp\left(-E^{\pm}_{\phi\to\chi}/k_BT\right) \quad H1 \tag{13}$$

$$k_{da} = k^{KTG}_{g\to\phi}\left(\frac{A_{st}}{A_{uc}}\right)\exp\left(\frac{\Delta S^{\neq}_{\phi\to\chi}}{k_B}\right)\exp\left(-\frac{\Delta H^{\neq}_{\phi\to\chi}}{k_BT}\right) \quad H1bis \tag{14}$$

With the assumption of stationary surface coverage by the physisorbed mobile molecular hydrogen (see [24] Fig. 6.1 and Eqs. (6)–(20), p. 219), any impinging molecule may either desorb or dissociate so that the probability to stick at a given site is expressed by Eq. (15), where $k_{\phi\to g}$ follows Eq. (7), and finally k_{da} follows Eq. (16), denoted model H2:

$$\frac{St(T)}{\left(\frac{A_{st}}{A_{uc}}\right)} = \frac{k_{\phi\to\chi}}{k_{\phi\to\chi} + k_{\phi\to g}} \quad \text{H2} \tag{15}$$

$$k_{da} = \left(\frac{A_{st}}{A_{uc}}\right)\frac{k_{\phi\to\chi}}{k_{\phi\to\chi} + k_{\phi\to g}} k^{KTG}_{g\to\phi} \quad \text{H2} \tag{16}$$

Another approach assumes the validity of the steady-state approximation, i.e. a dynamical system minimizing entropy production through serial steps satisfying microscopic reversibility (see [24] Eq. (2.47), p. 30). The equivalent forward microscopic rate constant for adsorption from gas phase to the chemisorbed state is identified to the harmonic mean of $k^{KTG}_{g\to\phi}$ and $k_{\phi\to\chi}$, so that k_{da} is now expressed by Eq. (17). We denote this model as H3.

$$k_{da} = \left(\frac{A_{st}}{A_{uc}}\right)\frac{k_{\phi\to\chi}}{k_{\phi\to\chi} + k^{KTG}_{g\to\phi}} k^{KTG}_{g\to\phi} \quad \text{H3} \tag{17}$$

Finally, it is possible to assume that thermodynamical equilibrium is always reached between gas phase and the physisorbed state, so that the surface coverage θ_{H_2} of the available 100%S Mo-edge initial surface follows the Langmuir isotherm, Eq. (18), where P_{H2} is the partial pressure of dihydrogen in gas phase, and $k^{KTG}_{g\to\phi}$ and $k_{\phi\to g}$ follow Eqs. (1) and (7), respectively. The probability k_{da} that a dissociative chemisorption event happens at any site within one second will then be merely the composition of spatial and temporal independent probabilities, namely the product of site occupation θ_{H_2} (adimensional) and rate $k_{\phi\to\chi}$ (s^{-1}). We denote further this model as H4, Eq. (19).

$$\theta_{H2} = \frac{\left(k^{KTG}_{g\to\phi}/k_{\phi\to g}\right)}{1 + \left(k^{KTG}_{g\to\varphi}/k_{\phi\to g}\right)} \tag{18}$$

$$k_{da} = \left(\frac{A_{st}}{A_{uc}}\right)\theta_{H2} k_{\phi\to\chi} \quad H4 \tag{19}$$

Notice that for $k^{KTG}_{g\to\phi}$ small compared to $k_{\phi\to g}$, and $k_{\phi\to g}$ large compared to $k_{\phi\to\chi}$, models H2 and H4 converge.

The order of magnitudes of $k^{KTG}_{g\to\phi}$, $k_{\phi\to g}$ and $k_{\phi\to\chi}$ prevailing for dihydrogen in our case in the temperature range considered, namely, in s^{-1}, are, respectively $[10^6–10^8]$, $[10^6–10^{13}]$ and $[2\times10^{-6}–4\times10^3]$. Therefore H_2 dissociation appears as a very rare event compared to both physisorption and its reverse process. In results section, we try to discriminate between models H1 to H4, looking for both physical consistency and the ability of these models to reproduce TPR experiments, provided that dissociative adsorption emerges as the rate-limiting step (*rls*). If not, equations analogous to 7 and 8, following TST, can be used in the TPR simulation, provided the enthalpic and entropic barrier for the actual *rls* elementary process can be determined from first principles.

2.2.2. First principles calculations of configuration energies and activation barriers

All first principles calculations were based on the density functional theory. To solve the Kohn–Sham equations [29] the Vienna *Ab Initio* Simulation Package (VASP) [30,31] is used. Exchange correlation energy is approximated within the Generalized Gradient Approximation (GGA), with the Perdew–Wang 91 [32] functional. Electron–ion interactions are described with the PAW method [33]. A plane wave basis set is used to develop the monoelectronic wavefunctions, truncated with a 337.0 eV cutoff. The Brillouin zone is sampled with a $4\times3\times1$ *k*-point meshing. The geometry optimization is completed when the convergence criteria on forces become smaller than 0.05 eV/Å. Barriers have been computed with the Nudged Elastic Band (NEB) method [34,35], as implemented in VASP. The Transition States (TS) have been confirmed as exhibiting a single imaginary vibrational frequency, according to frequency calculations based on numerical differentiation of force matrices, including optimized degrees of freedom. In order to reduce the computation cost of frequency calculations, the latter were performed with a reduced number of relaxing atoms: hydrogen atoms, sulfur atoms from dimers involved in the H_2 dissociative adsorption, and molybdenum atoms carrying the sulfur dimers and the sulfur atoms in between.

The atomistic modeling of MoS_2-based hydrotreating catalysts has seen several proposals [36–41] before the model proposed by Raybaud et al. [5] was acknowledged as a good reference starting point. From both *ab initio* molecular dynamics and DFT calculations, these authors have shown that a cleavage along the crystallographically well-defined planes $(1\,0\,\bar{1}\,0)$ and $(\bar{1}\,0\,1\,0)$ of 2H-MoS_2 is stable and undergoes only small relaxations even at a temperature of 700 K [42]. The three-dimensional periodic slab model proposed contains three layers of Mo atoms in the *x* direction, four layers in the *y* direction, and two layers in the *z* direction. It also contains a 12.8 Å vacuum layer along the *y* direction to isolate the edges from the neighboring slabs. The two inner layers are fixed to simulate the bulk MoS_2 constrain, while the upper and lower layers are allowed to relax. This model leads to a good agreement between computed and experimental interatomic distances. Therefore we based our DFT model on this work. In a first approximation we can consider that the single layers are chemically isolated and easily exfoliated. For this reason we considered single

layers of Mo-edge and S-edge separately; moreover we extended the layer in the *x* direction. Fig. 1 represents the cell used, with 4 Mo atoms in the *x* direction, 4 Mo atoms in the *y* direction, and 1 Mo atom in the *z* direction. Furthermore, according to the initial conditions of TPR experiments (starting after sulfidation under pure H_2S diluted in dinitrogen), the thermodynamically stable Mo-edge is covered by S_2 dimers, as explained in [14].

2.2.3. Analytical modelization of TPR experiments

Temperature-programed reduction (TPR) experiments are used to explore the reactivity of a solid with respect to a gas. Basically a substrate is dynamically equilibrated with a flowing gas mixture at a given initial temperature, determining an initial coverage of the surface by sorbates. The system is then heated according to some temperature program, and the change in gas phase composition is determined continuously during the heating sequence, yielding information about the change in solid composition.

According to the Redhead model [43], whenever desorption occurs only in the temperature-programed desorption case (TPD), the macroscopic desorption rate (or flux) r_{des} may be directly linked to the instantaneous residual coverage by adsorbates, θ_{ads}, according to an empirical *n*-order relationship, Eq. (20):

$$r_{des}(t) = k_{des}(t)\theta_{ads}^{n}(t) = -\frac{d\theta_{ads}(t)}{dt} \tag{20}$$

where *n* is the order of the desorption process with respect to coverage, and *t* is the time. While k_{des} increases with an increasing temperature, θ_{ads} decreases; as a consequence r_{des} goes through a maximum. TPD spectra are dependent on the initial coverage θ_0 and on the heating program. With a linear temperature program ($T = T_0 + \beta t$), one fixes the heating rate β (K s^{-1}) and the initial temperature T_0 to determine the change of temperature *T* with elapsed time *t*.

Here we generalize the Redhead model to TPR, by considering the rate $r_{rls}(t)$ (in mol g^{-1} s^{-1}) of the kinetically limiting step to reduction, and the associated microscopic rate k_{rls}.

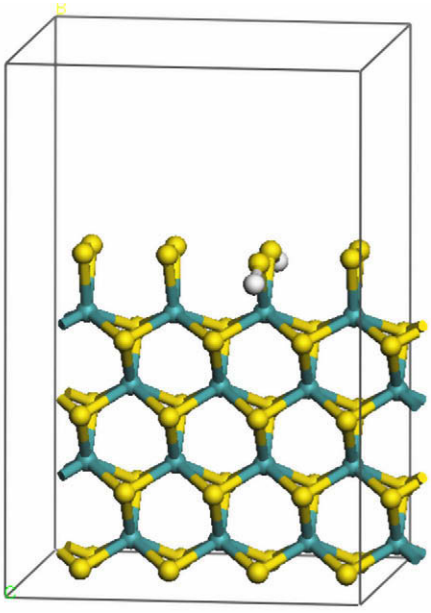

Fig. 1. A typical periodic slab model for MoS_2 Mo-edge, showing coverage of three top sites by S_2 dimers and one by a dimer hydrogenated into two geminal sulfhydril groups. Legend: black spheres (turquoise): molybdenum atoms, gray spheres (yellow): sulfur atoms, white spheres: hydrogen atoms. (For interpretation of the references to colour in this figure legend, the reader is referred to the web version of this article.)

Eq. (20) can be transposed into Eq. (21), replacing k_{des} by k_{rls}, and assuming that the rate-limiting step is first order with respect to density of unreacted sites θ^*:

$$r_{rls}(t) = k_{rls}(t)\theta^*(t) = -\frac{d\theta^*(t)}{dt} \tag{21}$$

Integration of Eq. (21) determines θ^*, Eq. (22), with θ_{Moe} the initial density of unreacted sites.

$$\theta^*(t) = \theta_{Moe}\exp\left(\int_o^t k_{rls}(x)dx\right) \tag{22}$$

In a typical experiment, which involves a flow of reducing mixture (e.g. H_2 diluted in an inert gas) across a thin layer of powdered catalyst, forming a pseudo-steady state isothermal differential reactor, the gas phase composition is monitored at both inlet and outlet, allowing to record either the instantaneous molar H_2 consumption or H_2S production, and to deduce from a mass balance the change of composition of the solid. Since one H_2 is consumed to reduce each S_2 dimer initially on top of an edge Mo into one bridging S and one desorbing H_2S, the integral quantity $Q_{cons\_H2}(t)$ given by Eq. (23) represents the hydrogen consumed (i.e. H_2S production), in mol g^{-1} at time *t*:

$$Q_{cons\_H_2}(t) = \theta_{Moe}\int_0^t k_{rls}(y)\exp\left(\int_0^y k_{rls}(x)dx\right)dy \tag{23}$$

$$Q_{cons\_H_2}(T) = \theta_{Moe}\int_{T_{\min}}^T k_{rls}(y)\exp\left(1/\beta\int_{y_{\min}}^y k_{rls}(x)dx\right)dy \tag{24}$$

$$\theta(T) = \left(1-\frac{\theta^*_{Mo}}{\theta_{Moe}}\right) = \int_{T_{\min}}^T k_{rls}(y)\exp\left(1/\beta\int_{y_{\min}}^{y_x} k_{rls}(x)dx\right)dy \tag{25}$$

The TPR profile can be alternatively expressed as a function of temperature, Eq. (24), and in terms of fractional degree of reduction, Eq. (25).

3. Results

3.1. Experimental results

3.1.1. Catalysts characterization

3.1.1.1. Textural properties, elemental XRF, and surface XPS analysis. The catalysts main characteristics are presented in Table 2.

Inspection of Table 2 reveals that up to Mo-12, the catalysts show a high and homogeneous dispersion of Mo in their oxidic precursor states. The surface area referred to the amount of support involved is unchanged within error margin of the BET method (SA of initial γ-alumina: 227 cm^2/g). For Mo contents above 16 wt%, however, poorly crystallized phases appear in minor amounts, MoO_3 first, then $Al_2(MoO_4)_3$, known to sulfide poorly.

For oxidic precursors, XPS spectra in the Mo binding energy range show only two broad lines centered at 232.8 eV (Mo $3d_{5/2}$) and 235.9 eV (Mo $3d_{3/2}$) corresponding to the presence of species involving only Mo^{+6} [44–46].

Catalysts sulfided in conditions similar to that in TPR experiments (Atmospheric pressure, 70 cm^3STP min^{-1} of flowing (15% vol $H_2S + H_2$) mixture, 2 h at 350 °C then cooling under flowing mixture) were analyzed by XPS for surface compositions in Mo^{4+}($3d_{5/2}$, 228.2 eV), Mo^{5+}($3d_{5/2}$, 230.4 eV) and Mo^{6+}($3d_{5/2}$, 232.8 eV) and S (2s, 226.2 eV). For this purpose, the Mo3d–S2s envelope was deconvoluted as mixtures of lorentzians (82%) and gaussians (18%), allowing unconstrained heights H for the main 3d5/2 or 2s lines, while other parameters were fixed: mid-height width (MHW) of 2.7, 2.7 1.5 and 2.3 eV, respectively, and coupled characteristics position/MHW/H to secondary Mo $3d_{3/2}$ lines, respectively, +3.2 eV/×1.3/×0.65, +3.2 eV/×1.3/×0.65 and +3.2

Table 2
Textural, chemical, and structural properties of studied catalysts (oxidic precursors). Microprobe column: RD stands for radial distribution, H stands for homogeneous.

Ref.	Mo XRF (wt%)	Pore volume ($cm^3\ g^{-1}$)	BET surface area ($m^2\ g^{-1}$)	Surface area per g of γ-Al_2O_3 ($m^2\ g^{-1}$)	Surface area per g oxidic precursor (SA from Eq. (20)) ($m^2\ g^{-1}$)	XRD of Mo phases A:% amorphous, B:%MoO_3, C:%$Al_2(MoO_4)_3$	Microprobe RD of Mo
Mo-4	4.2	0.71	225	236	213	A: 100	H
Mo-6	6.8	0.65	219	244	204	A: 100	H
Mo-9	9.8	0.55	208	244	193.5	A: 100	H
Mo-12	11.9	0.57	197	240	186	A: 100	H
Mo-17	16.1	0.52	178	235	172	B: 11; C: 0	H
Mo-20	18.2	0.50	167	229	164.8	B: 10; C: 0.5	H
Mo-22	22.5	0.56	168	253	150.1	B: 18; C: 15.5	H

eV/×1.0/×0.65. Table 3 collects XPS deconvolution results for sulfided catalysts.

Table 3 shows that above 16 wt% Mo, the degree of sulfidation is poorer, as could be expected from the occurrence of XRD detectable MoO_3 and $Al_2(MoO_4)_3$ phases.

3.1.1.2. TEM. Table 4 presents the results of TEM high resolution micrographs "manual" statistical analysis of MoS_2 nanoparticles "fingerprints" [47]. Representative histograms of slab lengths can be found as Supplementary material.

Table 4 reveals that while the average stacking number is fairly constant whatever the Mo content, the average particle width increases regularly with Mo content. Assuming that MoS_2 nanoparticles are related to the Mo^{4+} content, this trend would correspond to a fairly constant (within 30%) areal density of such nanoparticles of about 2 per 100 nm^2 of γ-Al_2O_3 support in sulfided catalysts, whatever the Mo content.

3.1.2. Temperature-programed reduction

TPR spectra obtained for catalysts Mo-4, Mo-9, Mo-12, Mo-20, Mo-22 and γ-alumina (blank) are presented in Fig. 2. Although TPR experiments were continued up to 1173 K, we focus here on the first "narrow" H_2 consumption/H_2S production peak observed below 600 K in all cases. Between 600 and 1173 K "broad" peaks were also observed, with an increasing integral area with Mo content. According to the energy required for removing one S atom from the Mo-edge with 50% coverage [6,15], we can only attribute these broad peaks to the further stages of reduction of the supported MoS_2 nanocrystallites, including S depletion first from Mo-edges from 50% to 0% coverage, then from the most stable basal planes. The onsets of these further stages appear in Fig. 2 between 600 and 680 K. Their analysis is, however, beyond the scope of the present report. The raw data obtained for catalysts have been corrected by substraction of the minor but non-zero rate of H_2 consumed by γ-alumina. Fig. 3 presents the TPR spectra corrected for the baseline drift corresponding to the onset of the higher temperature peak(s). For the purpose of this correction, instead of attempting a more sophisticated deconvolution, an amount increasing linearly with temperature and proportional to the difference between consumption at 590 K and 350 K was arbitrarily substracted to spectra in Fig. 3.

In Table 5 the corresponding peak temperatures, integral amounts of H_2 consumed at 600 K, and the resulting ratio S/Mo^{4+} eliminated by this first TPR peak, which we can identify with the ratio α of Mo edge sites to Mo involved in MoS_2 nanoparticles are presented. From Fig. 3 and Table 5, it can be concluded that while the TPR peak temperature increases with decreasing Mo^{4+} content, the edge to basal area ratio α of MoS_2 nanoparticles decreases with increasing Mo^{4+} content, as could be expected from the nearly constant MoS_2 area density revealed by the TEM results interpretation given in Table 4.

Knowing the Hydrogen partial pressure imposed during TPR experiments (5% H_2 in Ar at atmospheric pressure, therefore P_{H_2} = 5000 Pa), the mass of H_2, the heating rate β (10 K min^{-1}), the area of one Mo edge site ($\sim 9 \times 10^{-20}\ m^2$), the remaining unknowns in Eq. (24) are the barriers and energy differences intervening in k_{rls}. The results presented in the next section provide the desired input from first principles simulations.

3.2. Simulation results

3.2.1. DFT study of the Mo-edge reduction pathway from 100% to 50%S coverage

In order to address correctly the modeling of TPR experiments, we studied by DFT the reaction pathway corresponding to the reduction by H_2 of S_2 surface dimers on a fully sulfur covered (100%S) Mo-edge into bridging S adatoms, producing H_2S. As seen above, this state corresponds indeed to the one predicted by theory and confirmed by STM experiments in the conditions of high chemical potential of sulfur prevailing at the end of the presulfidation stage in our TPR experiments. Furthermore, detailed DFT calculations recently extended this conclusion to the case of γ-Al_2O_3 supported nanocrystallites, showing that a high chemical potential of sulfur and whatever their size, they lie with their basal planes parallel to the support surface, exchanging van der Waals interaction with the latter, without residual Mo–O bonds [49,50]. It

Table 3
XPS deconvolution analysis results for the sulfided catalysts.

Ref.	Mo^{4+} (%)	Mo^{5+} (%)	Mo^{6+} (%)	$(S/Mo^{4+})_{at}$	$(S/Mo_{tot})_{at}$ XPS	$(S/Mo_{tot})_{at}$ XRF (bulk)
Mo-4	84	9	7	2.1	1.8	1.8
Mo-6	85	8	6	2.1	1.8	1.8
Mo-9	92	4	4	1.9	1.8	1.8
Mo-12	93	0	7	1.8	1.7	1.7
Mo-17	94	0	6	1.7	1.6	1.6
Mo-20	93	1	5	1.6	1.5	1.5
Mo-22	93	0	7	1.5	1.4	1.4

Table 4
TEM analysis of MoS_2 nanoparticles in the sulfided catalysts. N stands for the number of particles observed for each sample; $\langle L \rangle$ is the average diameter (MoS_2 nanoparticles are detected when parallel to the electron beam, therefore L is an average length of dark fringe); $\langle n \rangle$ is the average number of stacked MoS_2 nanoparticles. GM refers to the geometrical model of [3], and α is the ratio of Mo atoms at the edge Mo^e over the total number of Mo atoms per nanoparticle.

Ref.	Mo XRF (wt%)	Mo^{4+}XPS (%)	N	$\langle L \rangle$ (nm)	$\langle n \rangle$	MoS_2 area density ($nm^{-2} \times 100$)	α (Mo^e/Mo) GM (at.at^{-1})
Mo-4	4.2	84	280	2.1	1.3	1.76	0.57
Mo-9	9.8	92	302	2.6	1.4	2.46	0.54
Mo-12	11.9	93	335	2.9	1.5	2.15	0.50
Mo-20	18.2	93	290	3.3	1.4	2.44	0.47
Mo-22	22.5	93	285	3.7	1.6	1.95	0.44

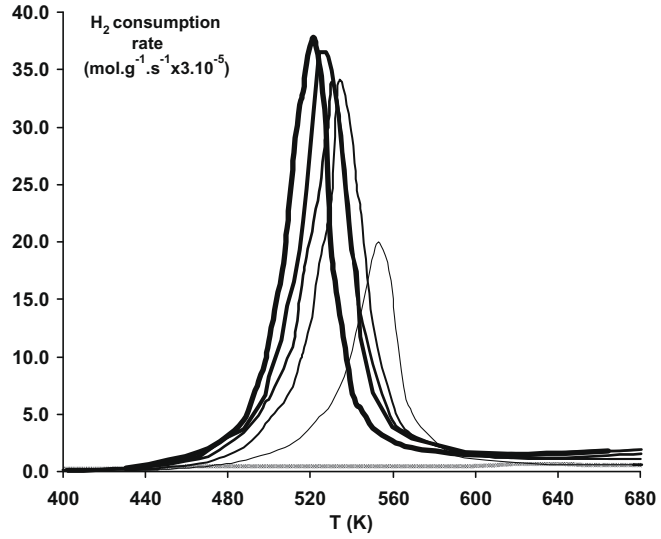

Fig. 2. Experimental TPR spectra for catalysts Mo-22, Mo-20, Mo-12, Mo-9, Mo-4, and γ-Al_2O_3 (from left to right, alternatively thick and thin black lines, γ-Al_2O_3 in thick gray line).

turned out that this pathway is rather complex with three consecutive sequences. First H_2 physisorbs without barrier and dissociatively adsorbs on neighboring sulfur dimers, with one hydrogen by sulfur dimer, forming two adjacent S–Mo–SH surface groups in mutual interaction via S···H–S hydrogen bonds. Then one H atom hops from one S–Mo–SH group to the other forming a SH–Mo–SH group and leaving a restored dimer. This SH–Mo–SH group is in a trans-configuration with an internal H–S···H–S hydrogen bond. From this state, either a SH rotates around the Mo–S bond and stabilizes the system in a cis-SH–Mo–SH group, or H_2S associatively desorbs. The results are schematized in Fig. 4. Along this non-intuitive pathway, the crucial role of S···H–S hydrogen bonds favoring hydrogen transfers is worth being highlighted.

The activation of the H-hopping step via TS2 requires an energy of 0.80 eV, the SH-rotation step via TS4 has a 0.39 eV barrier, and the associative H_2S desorption step via TS3 a 0.73 eV barrier. In regard to these values, the dissociative chemisorption of H_2 via TS1

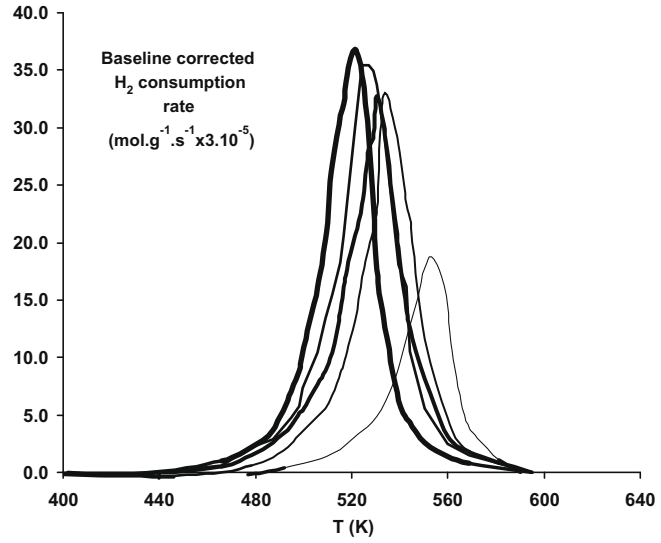

Fig. 3. Corrected TPR spectra for catalysts Mo-22, Mo-20, Mo-12, Mo-9, and Mo-4 (from left to right, alternatively thick and thin lines).

Table 5
First peak temperatures and edge to basal area ratios α deduced from TPR experiments.

Ref.	Mo^{4+} (wt%)	T peak (K)	H_2 consumed below 600 K (μmol g^{-1})	$\alpha = S/Mo^{4+}$
Mo-4	3.53	552	128	0.348
Mo-9	9.02	533.5	223	0.237
Mo-12	11.07	530.4	248	0.215
Mo-20	16.93	527.4	273	0.153
Mo-22	20.92	521.2	289	0.133

can be considered as the rate-limiting step for the hydrogenation of the surface, with a 0.95 eV barrier. In what follows, we consider therefore the rate-limiting step of TPR to be the dissociative adsorption of H_2, so that k_{da} expressed according to any model H1 to H4 replaces k_{rls} in Eqs. (21)–(25).

Table 6 presents the calculated normal mode frequencies, for the vibrations associated to configurations involved in the dissociative H_2 adsorption: physisorbed state, TS1, and the two S–Mo–SH groups in mutual interaction via hydrogen bonds. These frequencies permitted to determine the corresponding vibrational entropy and energy changes as a function of temperature according to Eqs. (SI1) and (SI2) reported in Supplementary material.

3.2.2. Analytical modelization of TPR experiments

In this section we try to discriminate between models H1 to H4 for the description of H_2 dissociative adsorption.

In the cases where the entropy change in the H_2 dissociation process from the physisorbed state to the transition state $\Delta S^{\neq}_{\phi\to\chi}$ is taken into account (models H1bis to H4), the theoretical peak temperatures and shapes of TPR spectra turn out to be very sensitive to this quantity, and its variation with temperature. On the one hand, we have no theoretical input for f, the fraction of translational–rotational entropy of gaseous H_2 retained upon physisorption (Eq. (4)). On the other hand, we found that good fits in both peak temperature and shapes were obtained only for entropy variations $\Delta S^{\neq}_{\phi\to\chi}$ increasing with increasing temperature ($\Delta S^{\neq}_{\phi\to\chi}$ becoming less negative, and lower in absolute value, so that the entropy loss upon the activation of the dissociation process decreases as temperature increases). Theory from Eqs. (SI1)–(SI6) reported in Supplementary material, and (3) and (4) predicts a slight, almost linear decrease with increasing temperature assuming constant f, and the set of vibration frequencies computed with the particular models chosen. Therefore, the inverse tendency is possible only if, as the reduction proceeds and the initially 100%S Mo-edge gets progressively depleted in S_2 dimers, f decreases, i.e. less translational-rotational entropy is carried by dihydrogen from gas phase to the physisorbed state.

Therefore, taking 375 K for the common onset of S-edge depletion in our TPR experiments, we have assumed that $f[T, \theta_S(T)]$ varies linearly with T during the TPR experiment, according to Eq. (26), where a is a positive constant:

$$f(T) = f(375K) - aT \tag{26}$$

Parameters a and f(375 K) are allowed to vary freely so as to minimize the root mean square deviation between theoretical prediction and experimental data points for one catalyst (arbitrarily chosen as M22). A consistency criterion is provided by a simple physical constraint on f (375 K) and a: the adimensional fraction $f(T)$ should be always higher than or equal to zero, and lower than or equal to one. In practice, we impose the restraint $f(600\,K) \geqslant 0$, since all TPR peaks are back to the baseline above 600 K, implying that Mo-edges are now at 50%S coverage.

According to this fitting procedure, the theoretical predictions following H1 to H4, with input from our DFT calculations, are

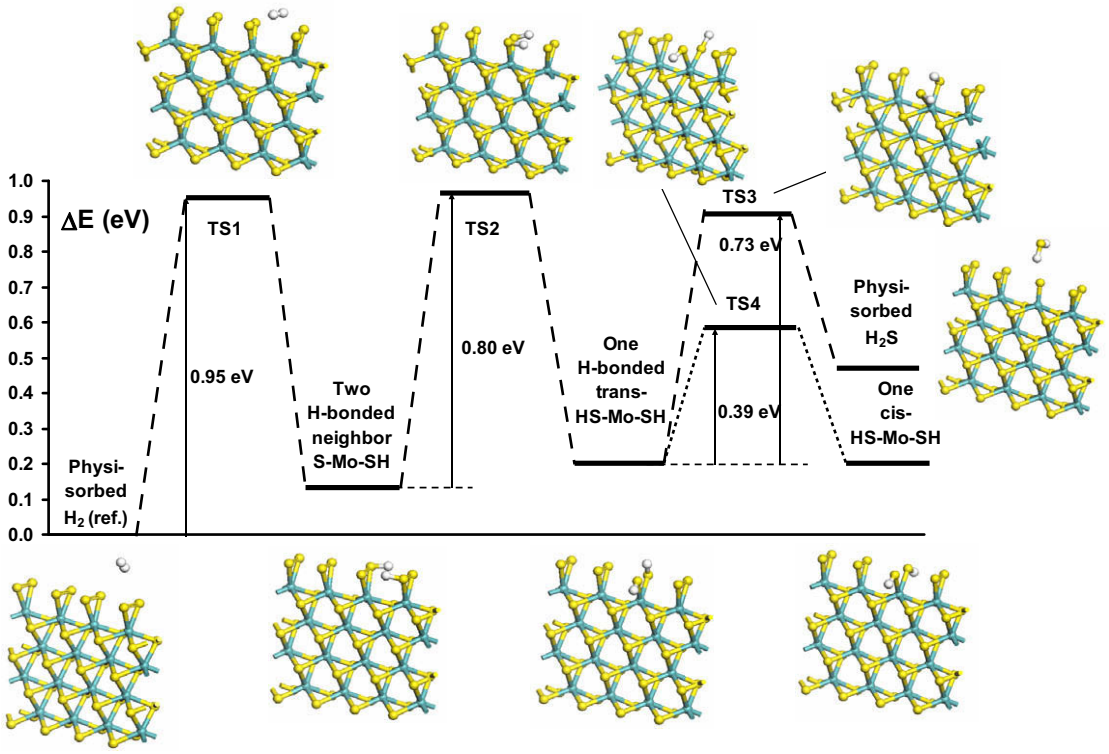

Fig. 4. Energy profile along the pathway starting with H_2 dissociative adsorption and ending in H_2S associative desorption. Configurations corresponding to intermediate and transition states are represented as balls and sticks. Legend: turquoise spheres: molybdenum atoms, yellow spheres: sulfur atoms, white spheres: hydrogen atoms. (For interpretation of the references to colour in this figure legend, the reader is referred to the web version of this article.)

Table 6
Normal modes frequencies in units of cm^{-1} for the H_2 dissociative adsorption process. From the local minimum of the physisorbed state (H2_Phys), the system is passing by the transition state TS1 exhibiting one negative frequency, then relaxes to another local minimum with dissociated hydrogen shared between two S–Mo–SH groups.

H2_Phys	4274	596	595	390	378	349	329	328	320	305
	274	271	243	226	210	199	178	175	169	156
	155	147	135	129	125	85	70	66	64	57
TS1	3492	804	787	756	549	547	385	373	368	340
	322	313	304	279	265	259	231	219	197	190
	178	172	163	143	137	117	111	99	66	−182
2 S–Mo–SH	2157	2143	893	869	624	609	511	506	390	378
	345	331	322	307	285	276	235	232	219	196
	185	182	166	154	130	125	112	102	75	65

compared to experiment M22 in Fig. 5a–d, and the corresponding fitting parameters and figures of merits are presented in Table 7.

Model H1 (Fig. 5a) is obviously in large error, failing to predict both the peak temperature and the peak shape (root mean square relative deviation, rmsrd = 54.7%). However, the peak temperature being very sensitive to the value of the chemisorption energy barrier, it is well predicted if the DFT number is corrected by only −0.05 eV (Fig. 5b), while the peak shape remains poorly predicted (rmsrd = 94%).

Model H1bis (Fig. 5c) may achieve an excellent fit of the experimental results (rmsrd = 11.6%), but with unphysical parameters: $f(375\ K) = -0.23$ and $a = 1.97 \times 10^{-3}\ K^{-1}$ determining $f < 0$ for all temperatures, therefore an inconsistency since more translational–rotational entropy would appear in the physisorbed state than in the gas state.

No constrained solution could be found for models H2 and H4: we can therefore rule them out. Indeed, Eq. (8), which ensures microscopic reversibility in coherence with Eq. (4), determines much too low sticking coefficient or coverages in the temperature range 375–600 K of experimental TPR peaks to allow significant dissociation rates.

Finally, model H3 achieves an excellent fit (Fig. 5d) (rmsrd = 11.7%), with on average $f(375\ K) = 0.514$ and $a = 2.08 \times 10^{-3}\ K^{-1}$, allowing all constraints to be satisfied.

For model H3, $f(375\ K)$ and a values are quite similar for all catalysts (standard deviations 0.04 and $1.6 \times 10^{-4}\ K^{-1}$, respectively), and we notice no systematic trend with varying Mo content in catalyst. Since experimentally determined parameters influence the prediction through Eqs. (11) and (12), the slight spread may come from cumulated slight random experimental errors.

On the basis of these results, we retain H3 as the best description of dissociative adsorption in our experimental conditions: the comparison between experimental results and predictions of this analytical model for all catalysts are presented in Fig. 6.

4. Discussion

The most salient finding we report, is the high sensitivity of TPR experiments performed with sulfided MoS_2-based supported catalysts, in terms of initial peak temperature and shape, on the loading, dispersion, and sulfidation state of MoS_2 nanoparticles. We show that these peak profiles and positions can be interpreted theoretically very accurately, but this interpretation is extremely sensitive to the temperature dependence of the free-energy change associated to the rate-limiting step barrier. As long as suitable atomistic models can be elaborated, first principles calculations do provide reliable estimates of the energetic and vibrational components of this critical function, but so far, the translational–rotational part remains elusive for want of reliable theoretical models for the physisorbed and transition states. Therefore, instead of a full first principles theoretical representation of TPR spectra, we

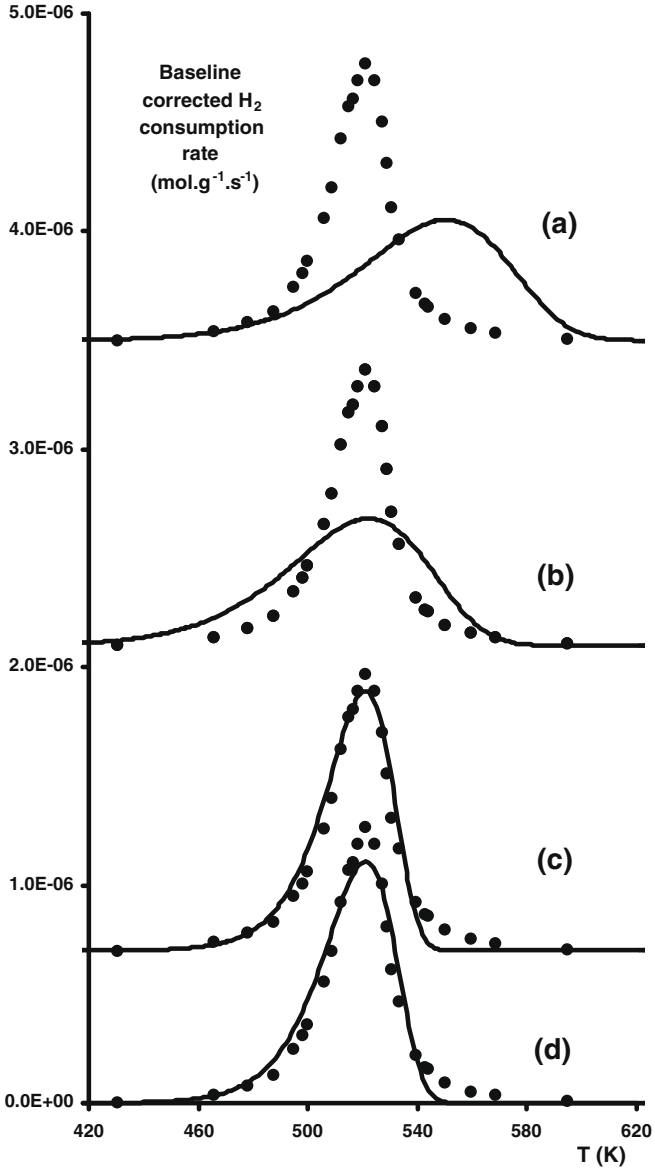

Fig. 5. Theoretical (full lines) and experimental (dots) TPR spectra for catalyst Mo-22: from top to bottom, models H1 (a), H1 with corrected barrier (b), H1 bis (c), and H3 (d).

have proposed a fitting strategy leaving two parameters free, but subject to a physical constraint of consistency.

Following this fitting strategy, we have selected the H3 model as yielding the most consistent theoretical description of TPR spectra. This model relies on the hypothesis of minimum entropy production along processes occurring in series, which is actually the basis of the rate limiting step assumption commonly used in microkinetic models. We describe therefore dissociative adsorption of H_2 as physisorption and activated dissociation in series, forming the overall rate-limiting step. We believe this description is very appropriate for TPR experiments performed as in our case in a dynamical fashion, with a differential crossed fixed-bed at fixed flow rate of reducing gas.

We must concede that the exclusion, according to our strategy, of models H2/H4 and H1bis, holds under the assumption that numbers provided by DFT are accurate enough. Although the energy barrier (0.95 eV) can be considered as accurate within 0.02 eV, the frequencies of the soft normal modes might be in systematic

Table 7
Comparison of the performances of models H1 to H3 used in the expression of dissociative adsorption rates, when comparing theoretical and experimental TPR spectra. Models H1bis and H3 provide excellent fits as indicated by the lower mean square deviations (rmsd in %), but only for H3 are the fitting parameters f(375 K) and a physically meaningful. No constrained solutions could be found for models H2 and H4. (1) Squared coefficient of correlation between predicted and experimental peak temperature; (2) slope of the linear regression T_{peak}(Pred.) = m T_{peak} (Exp); (3) fraction f (Eq. (4)) of translational–rotational entropy of gas phase H_2 retained in the physisorbed state on the 100%S Mo-edge surface, determined as the first free parameter in the fitting of model to experimental TPR spectrum. (4) slope a of the assumed linear relationship between $f(T)$ and temperature T, determined as the second free parameter in the fitting procedure (K^{-1}).

Model	H1	H1corr	H1bis	H3
k_{da} (s^{-1})	Eq. (13)	Eq. (13)	Eq. (14)	Eq. (17)
$E^{\neq}$ (eV)	0.95	0.8767	0.95	0.95
rmsrd (%)	54.52	140.59	10.3	10.1
T peak $R^{2\ (1)}$	0.2848	0.1793	0.9866	0.9917
T peak $m^{(2)}$	1.0599	0.9798	1.0013	1.0009
f(375 K) Mo-22$^{(3)}$	–	–	–0.220	0.482
f(375 K) Mo-20$^{(3)}$	–	–	–0.236	0.520
f(375 K) Mo-12$^{(3)}$	–	–	–0.270	0.485
f(375 K) Mo-9$^{(3)}$	–	–	–0.249	0.508
f(375 K) Mo-4$^{(3)}$	–	–	–0.180	0.574
Average f(375 K)	–	–	**–0.231**	**0.514**
Std. dev. f(375 K)	–	–	**0.068**	**0.037**
a Mo-22$^{(4)}$	–	–	0.00234	0.00214
a Mo-20$^{(4)}$	–	–	0.00199	0.00218
a Mo-12$^{(4)}$	–	–	0.00175	0.00192
a Mo-9$^{(4)}$	–	–	0.00171	0.00190
a Mo-4$^{(4)}$	–	–	0.00205	0.00225
Average a	–	–	**0.00197**	**0.00208**
Std. dev. a	–	–	**0.00025**	**0.00016**

error since they were computed assuming harmonic potentials. Anharmonic corrections generally decrease raw DFT frequencies by a few% (see, for instance [48]). However, allowing as another free parameter in the fit a correction applied to all frequencies, allows finding physically acceptable solutions: an optimum is found for +65 cm^{-1} for models H2 and H4, but with very poor fits (rmsrd = 84% and 122%, respectively). Such a correction amounts, however, to more than 50% of the softer modes frequencies which dominate the vibrational entropy change. Similar results are obtained when all frequencies are corrected by a constant factor λ. We find optimally for H2, λ = 1.77, rmsrd = 37%, for H4, λ = 1.36, rmsrd = 27% and for H1bis, λ = 1.52, rmsrd = 10.8%. Such corrections are, however, quite large, and clearly not compatible with the accepted accuracy of DFT.

Finally, our analysis relies on the assumption that the reduction pathway illustrated in Fig. 4 remains unaffected either by the proximity of surface atoms belonging to the γ-Al_2O_3 support, or by the –SH groups or vacancies being proximal to S_2 dimers on the Mo-edges, as the extent of reduction proceeds. Since at least 0.3 nm separates the outmost O atoms of the support from the closest S of each edge capping dimer in the "flat lying" MoS_2 slab [49, see Figs. 4a and 6a], the first effect is unlikely. It is, however, likely that barriers to S_2 dimers reduction are affected by the close vicinity of already reduced sites: although we believe that the introduction of Eq. (26) accounts partly and empirically for this depletion effect, additional DFT calculations of the energy profile along the reduction pathway, starting with initial configurations modeling intermediate coverages between 100%S and 50%S, should shed light on this point. We hope to report the results of such very extensive calculations in the near future. It can be expected, however, that such effects would be all the more manifest as the edges coverage by sulfur approaches 50%, or in other terms capping S_2 dimers become more dilute and the probability that they are surrounded by Mo–SH or Mo–S–Mo groups is higher. This might explain in particular the systematic discrepancy between predicted and

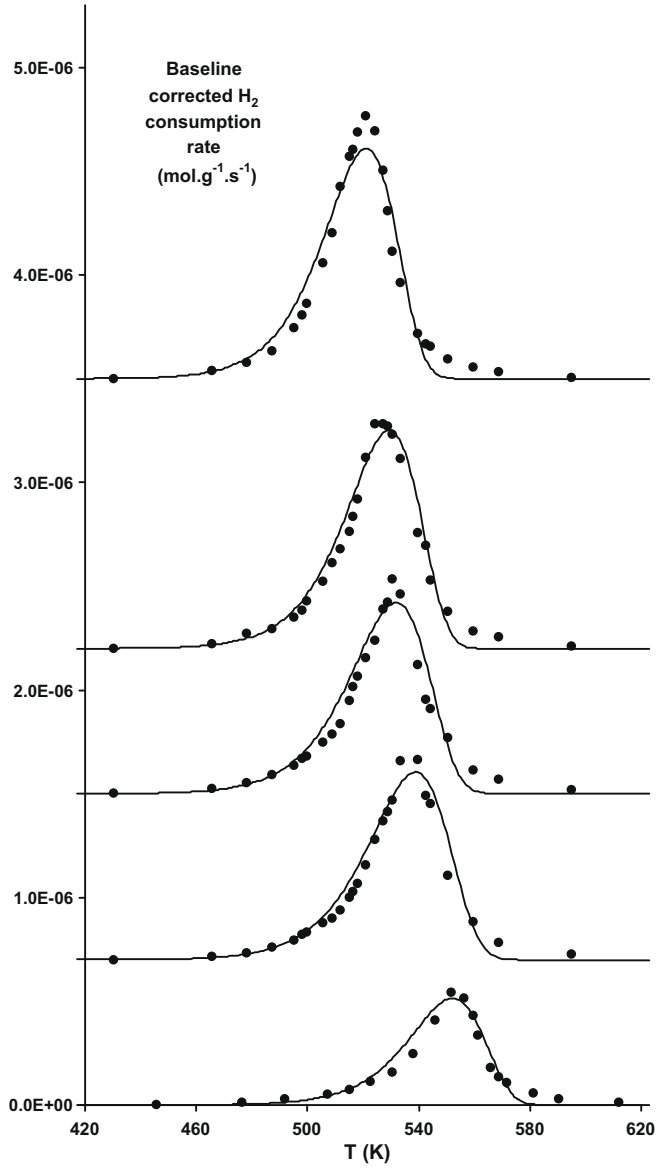

Fig. 6. Theoretical (full lines) and experimental (dots) TPR spectra for, from top to bottom, catalysts Mo-22, Mo-20, Mo-12, Mo-9, and Mo-4. The theoretical spectra correspond to the overall best fit using model H3.

experimental TPR spectra tails, which is apparent in Fig. 6 beyond 560 K, i.e. as the fraction of residual S_2 dimers falls below 20%. This discrepancy on the high temperature side is indicative of a slower process on average, or higher barrier for the *rls*, with respect to the predicted value. It can be foreseen that as reduction proceeds, the pattern of competing elementary events becomes more complex, and less amenable to a simple description by one single rate-limiting step. We are currently developing kinetic Monte Carlo simulations of these phenomena, the results of which will be reported later, and which should help overcome the current shortcomings in our analysis.

5. Conclusions

In this report, we have specifically addressed the mechanism of reduction of sulfided γ-Al_2O_3 supported MoS_2 catalytic nanoparticles by dihydrogen gas, starting from the state 100% sulfur covered, and ending in 50% sulfur covered Mo-edges, with the production of gaseous hydrogen sulfide. This reaction corresponds to the first stage of hydrotreating catalysts activation, following presulfidation under high chemical potential of sulfur. Our investigation comprises an experimental part, with the preparation and characterization of a consistent set of oxidic catalysts precursors with variable loadings in Mo, presulfidation of these catalysts under high chemical potential of sulfur ensuring prevalence of 100%S covered Mo-edges (triangular nanoparticles), and finally the acquisition of temperature-programed reduction spectra. The theoretical part involves DFT calculations of the free-energy barriers along the reduction pathway, and elaboration of an analytical model of TPR spectra with first principles barriers and some measurable catalysts characteristics as inputs.

Our conclusions are the following:

1. Experimental TPR spectra present a distinct narrow first peak, which we attribute to the reductive transition from 100%S covered Mo-edges to 50%S covered Mo-edges.
2. The peak temperatures are in the range 520–560 K for catalysts of content in Mo varying between 4 and 22 wt%, and these increase as Mo content decreases.
3. The peak integrals convey a direct information on the sulfided catalyst's dispersion (ratio α = Mo-edge/Mo_total).
4. The reduction pathway starts with the physisorption of dihydrogen between two capping S_2 pairs, proceeds to a rate-limiting dissociation via a transition state into adjacent mono-sulfhydrilated S_2 pairs in mutual hydrogen bonding situations, followed by a H transfer to one S_2 in the pair, resulting in a chemisorbed H_2S_2 species, followed by an activated transfer of one H to one S in the pair, leading to H_2S and S bonded to the same Mo edge atom, and finally followed by the activated desorption of H_2S and bridging of the remaining S ad-atom between adjacent Mo edge atoms.
5. The rate-limiting hydrogen dissociation total energy barrier is 0.95 eV, while the free-energy barrier is of the order of 1.5 eV.
6. Within the level of theory implemented, and the limitations of atomistic models used to represent initial and transition states, since translational–rotational entropy contributions in physisorbed and transition states are not well described theoretically, fully first principles predictions of the entropic barriers and their temperature dependence were not possible, although critically determining both peak TPR temperatures and TPR spectra profiles.
7. We have, however, developed a fitting scheme with a consistency criterion allowing reasonable arguments for clear discrimination between models.
8. According to this scheme, the most consistent model for dissociative adsorption from gas phase, corresponds to the pseudo-steady state approximation for physisorption and homolytic chemisorptive dissociation in series (H3).
9. The decrease in TPR spectra peak temperatures with increasing Mo content is very well explained by our model and simulations, as resulting mostly from an increase in the ratio A_{st}/A_{uc} of the area available for reactive adsorption over the total surface area. The loss of dispersion (decreasing α) with increasing Mo content is overcompensated by the increasing active Mo-edge area.

Acknowledgment

This work has been performed within the SIRE Project (Grant No. ANR-06-CIS6-014-04) sponsored by the Agence Nationale de la Recherche (ANR).

Appendix A. Supplementary material

Supplementary data associated with this article can be found, in the online version, at doi:10.1016/j.jcat.2009.07.017.

References

[1] J.F. Paul, S. Cristol, E. Payen, Catal. Today 130 (2008) 139.
[2] P. Raybaud, Appl. Catal. A Gen. 322 (2007) 76.
[3] S. Kasztelan, H. Toulhoat, J. Grimblot, J.P. Bonnelle, Appl. Catal. 13 (1984) 127.
[4] J.V. Lauritsen, M.V. Bollinger, E. Laegsgaard, K.W. Jacobsen, J.K. Norskov, B.S. Clausen, H. Topsoe, F. Besenbacher, J. Catal. 221 (2004) 510.
[5] P. Raybaud, J. Hafner, G. Kresse, H. Toulhoat, Phys. Rev. Lett. 80 (1998) 1481.
[6] P. Raybaud, J. Hafner, G. Kresse, S. Kasztelan, H. Toulhoat, J. Catal. 190 (2000) 128.
[7] E. Krebs, B. Silvi, P. Raybaud, Catal. Today 130 (2008) 160.
[8] J.V. Lauritsen, J. Kibsgaard, G.H. Olesen, P.G. Moses, B. Hinnemann, S. Helveg, J.K. Norskov, B.S. Clausen, H. Topsoe, E. Laegsgaard, F. Besenbacher, J. Catal. 249 (2007) 220.
[9] J.V. Lauritsen, M. Nyberg, J.K. Norskov, B.S. Clausen, H. Topsoe, E. Laegsgaard, F. Besenbacher, J. Catal. 224 (2004) 94.
[10] J.V. Lauritsen, S. Helveg, E. Laegsgaard, I. Stensgaard, B.S. Clausen, H. Topsoe, E. Besenbacher, J. Catal. 197 (2001) 1.
[11] S.M.A.M. Bouwens, J.A.R. van Veen, D.C. Koningsberger, V.H.J. De Beer, R. Prins, J. Phys. Chem. 95 (1991) 123.
[12] S.M.A.M. Bouwens, D.C. Koningsberger, V.H.J. De Beer, S.P.A. Louwers, R. Prins, Catal. Lett. 5 (1990) 273.
[13] S.M.A.M. Bouwens, R. Prins, V.H.J. De Beer, D.C. Koningsberger, J. Phys. Chem. 94 (1990) 3711.
[14] P. Raybaud, J. Hafner, G. Kresse, S. Kasztelan, H. Toulhoat, J. Catal. 189 (2000) 129.
[15] H. Schweiger, P. Raybaud, G. Kresse, H. Toulhoat, J. Catal. 207 (2002) 76.
[16] H. Toulhoat, P. Raybaud, S. Kasztelan, G. Kresse, J. Hafner, Catal. Today 50 (1999) 629.
[17] R.R. Chianelli, G. Berhault, P. Raybaud, S. Kasztelan, J. Hafner, H. Toulhoat, Appl. Catal. A Gen. 227 (2002) 83.
[18] P. Sabatier, Ber. Deutch. Chem. Ges. 44 (1911) 2001.
[19] H. Toulhoat, P. Raybaud, J. Catal. 216 (2003) 63.
[20] C.M. Weinert, M. Scheffler, in: H.J. von Bardeleben (Ed.), Defects in Semiconductors, Mater. Sci. Forum, vols. 10–12, 1986, p. 25.
[21] M. Scheffler, J. Dabrowski, Philos. Mag. A 58 (1988) 107.
[22] X.-G. Wang, W. Weiss, Sh.K. Shaikhutdinov, M. Ritter, M. Petersen, F. Wagner, R. Schlögl, M. Scheffler, Phys. Rev. Lett. 81 (1998) 1038.
[23] K. Reuter, M. Scheffler, Phys. Rev. B 73 (2006).
[24] R.A. van Santen, J.W. Niemantsverdriet, Chemical Kinetics and Catalysis, Plenum Press, New York, 1995.
[25] R.P. Marathe, J. Colloid Interf. Sci. 290 (2005) 69–75.
[26] H. Eyring, M. Polanyi, Z. Phys. Chem. Abt. B 12 (1931) 279.
[27] H. Eyring, J. Chem. Phys. 3 (1935) 107.
[28] M.G. Evans, M. Polanyi, Trans. Faraday Soc. 31 (1935) 875.
[29] W. Kohn, L.J. Sham, Phys. Rev. 140 (1965) A1133.
[30] G. Kresse, J. Furthmüller, Phys. Rev. B 54 (1996) 11169.
[31] G. Kresse, J. Furthmüller, Comput. Mater. Sci. 6 (1996) 15.
[32] J.P. Perdew, J.A. Chevary, S.H. Vosko, K.A. Jackson, M.R. Pederson, D.J. Singh, C. Fiolhais, Phys. Rev. B 46 (1992) 6671.
[33] G. Kresse, D. Joubert, Phys. Rev. B 59 (1999) 1758.
[34] G. Mills, H. Jonsson, Phys. Rev. Lett. 72 (1994) 1124.
[35] G. Mills, H. Jonsson, G.K. Schenter, Surf. Sci. 324 (1995) 305.
[36] S. Harris, R.R. Chianelli, J. Catal. 86 (1984) 400.
[37] S. Harris, R.R. Chianelli, J. Catal. 98 (1986) 17.
[38] M.C. Zonnevylle, R. Hoffmann, S. Harris, Surf. Sci. 199 (1988) 320.
[39] J. Joffre, P. Geneste, D.A. Lerner, J. Catal. 97 (1986) 543.
[40] C. Rong, X. Qin, J. Mol. Catal. 64 (1991) 321.
[41] R.P. Diez, A.H. Jubert, J. Mol. Catal. 83 (1993) 219.
[42] P. Raybaud, J. Hafner, G. Kresse, H. Toulhoat, Surf. Sci. 407 (1998) 237.
[43] P.A. Redhead, Vacuum 12 (1962) 203.
[44] J.N. Fiedor, A. Proctor, M. Houalla, D.M. Hercules, Surf. Interf. Anal. 20 (1992) 1.
[45] J.-G. Choi, L.T. Thompson, Appl. Surf. Sci. 93 (1996) 143.
[46] T.A. Patterson, J.C. Carver, D.E. Leyden, D.M. Hercules, J. Phys. Chem. 80 (1976) 1700.
[47] K.C. Pratt, J.V. Sanders, N. Tamp, J. Catal. 66 (1980) 82.
[48] P. Raybaud, M. Digne, R. Iftimie, W. Wellens, P. Euzen, H. Toulhoat, J. Catal. 201 (2001) 236.
[49] C. Arrouvel, M. Breysse, H. Toulhoat, P. Raybaud, J. Catal. 232 (2005) 161.
[50] D. Costa, C. Arrouvel, M. Breysse, H. Toulhoat, P. Raybaud, J. Catal. 246 (2007) 325.